RSC Advances

PAPER

View Article Online
View Journal | View Issue

Cite this: *RSC Adv.*, 2024, **14**, 13157

Regulating oxygen vacancies by Zn atom doping to anchor and disperse promoter Ba on MgO support to improve Ru-based catalysts activity for ammonia synthesis†

Yuanjie Chen,[a] Junqiao He,[a] Haiyan Lei,[a] Qunyao Tu,[a] Chen Huang,[a] Xiangwei Cheng,*[b] Xiazhen Yang,[a] Huazhang Liu[a] and Chao Huo *[a]

In heterogeneous catalysis, surface defects are widely regarded as an effective means to enhance the catalytic performance of catalysts. In this study, the oxygen vacancy-rich $Mg_{(1-X)}Zn_XO$ solid solution support was successfully prepared by doping a small amount of Zn into MgO nanocrystals. Based on this support, Ru/Ba–$Mg_{(1-X)}Zn_XO$ catalyst for ammonia synthesis was prepared. Characterization using TEM, EPR, XPS, and DFT calculations confirmed the successful substitution of Zn atoms for Mg atoms leading to the formation of more oxygen vacancies (OVs). N_2-TPD, SEM and TEM analyses revealed that a small amount of Zn had minimal influence on the surface morphology and the size of Ru nanoparticles. The abundance of OVs in the support was identified as the primary factor enhancing the catalytic activity. XPS, H_2-TPD and kinetics experiment studies further elucidated the mechanism by which OVs promote the reaction, with OVs serving as an anchor point for the promoter Ba on the MgO support and promoted the dispersion of Ba. This anchoring effect not only enhanced the electron density on Ru, favoring the dissociation of the N≡N bond, but also mitigated hydrogen poisoning. As a result,the ammonia synthesis rate reached 1.73 mmol g^{-1} h^{-1}. Furthermore, the CO_2-TPD and H_2-TPR analyses indicated that Zn doping effectively promotes the metal-support interaction (MSI) and surface alkalinity. The findings of this study offers valuable insights for the design of defective modified catalyst supports.

Received 27th February 2024
Accepted 15th April 2024

DOI: 10.1039/d4ra01517g

rsc.li/rsc-advances

1. Introduction

Ammonia synthesis technology, a crucial invention of the 20th century, sustains the food supply chain for about 40% of the global population.[1] Additionally, ammonia is regarded as a promising carbon-free energy support due to its high energy density (12.8 GJ m^{-3}) and high hydrogen storage capacity (17.8 wt%).[2,3] However, the conventional Haber–Bosch process, which employs Fe catalysts, operates under high temperature (>450 °C) and pressure (>20 MPa) conditions, consuming nearly 2% of the global energy and resulting in significant CO_2 emissions.[4] Consequently, there is an urgent need to develop advanced catalysts that exhibit high activity at low pressures to mitigate process costs and emissions. In the context of ammonia synthesis, nano-sized Ru metal particles possess a unique B_5 site structure, which can effectively adsorb and dissociate N_2. These particles exhibit superior catalytic efficiency compared to traditional Fe based catalysts, particularly under low pressure conditions. Therefore, the supported Ru catalyst is considered as the second generation ammonia synthesis catalyst.[5–9] Various materials, including nitrides,[10,11] perovskites,[12] carbon,[13,14] and metal oxides[15,16] have been developed as supports. Among these, MgO, due to its low cost, stability, and strong electron donating ability, is widely regarded as a promising support for Ru-based ammonia synthesis catalysts; and the alkaline earth metal Ba is one of the most effective promoters in Ru/MgO ammonia synthesis catalyst systems.[17–19] Despite this, the ammonia synthesis rate of Ru/Ba–MgO catalyst has not reached the standards required for industrial application. Researchers are therefore seeking to improve the activity of the catalyst by modifying the MgO support.[20–22]

In recent years, there has been growing interest in altering the properties of supports by introducing defects on their surfaces.[23–29] However, limited research has been conducted on the modification of MgO supports through surface defects. Oxygen vacancy (OVs), a type of surface defect, have effects on the stability of the support,[30] and change the acid-base site on the support surface to promote H_2 adsorption.[31,32] Furthermore, OVs facilitate electrons transfer from OVs to nitrogen molecules adsorbed on Ru nanoparticles (Ru NPs), which enhances the

[a]State Key Laboratory Breeding Base of Green Chemistry-Synthesis Technology and Key Laboratory of Green Chemistry-Synthesis Technology of Zhejiang Province, Zhejiang University of Technology, Hangzhou 310014, China. E-mail: chaohc@zjut.edu.cn
[b]Modern Educational Technology Experimental Center, Zhejiang Police College, Hangzhou 310053, China. E-mail: chengxiangwei@zjjcxy.cn

† Electronic supplementary information (ESI) available. See DOI: https://doi.org/10.1039/d4ra01517g

electron-donating capacity of Ru and promotes the dissociation of N≡N.[12,33] Atom doping, a prevalent technique for generating OVs,[34] involves the substitution of original metal cations with other metal atoms within the metal oxide support, thereby promoting the generation of OVs.[35]

In this work, we aimed to incorporate Zn atoms into MgO supports to generate OVs. Specifically, we examined the influence of Zn atoms doping on MgO supports and Ru/Ba–MgO ammonia synthesis catalysts, delving into the underlying mechanism. It was found that Zn atoms substituted Mg atoms in the MgO cubic crystal lattice, forming $Mg_{(1-X)}Zn_XO$ solid solution. The doping of Zn reduced the oxygen vacancy formation energy (E_{OV}) on the MgO crystal planes, leading to an elevated concentration of OVs. Additionally, these OVs served as anchor sites for Ba, enhancing its dispersion, This improved dispersion mitigated hydrogen poisoning and increasing the electron density of the active metal Ru, ultimately increasing the catalyst's ammonia synthesis rate.

2. Experimental procedures

2.1 Ba–$MgO_{(1-X)}Zn_XO$ synthesis

A certain amount of $Mg(NO_3)_2\cdot 6H_2O$ and $Ba(NO_3)_2$ was dissolved in 400 mL of deionized water, (maintaining a molar ratio of Ba to Mg of 1 : 5). Then the corresponding molar amount of $Zn(NO_3)_2\cdot 6H_2O$ was added into the above mixed solution and stirred until complete dissolution occurred. Following this, the alkaline precipitant was added to adjust the pH of the solution to 10.0. After ultrasonic treatment for 50 min, the solution was left standing for 24 h. Then Ba–$Mg_{(1-X)}Zn_XO$ with varying X values ($X = 0$, 0.01, 0.03, 0.05, 0.1, 0.15, 0.20 and 0.30, $X =$ the mole ratio of Zn/Mg) were obtained through extraction, filtration, washing and drying at 110 °C for 12 h, followed by calcination at 500 °C for 6 h.

2.2 $MgO_{(1-X)}Zn_XO$ synthesis

The procedure was the same as the above experiment, but without adding $Ba(NO_3)_2$.

2.3 Ru/Ba–$Mg_{(1-X)}Zn_XO$ and Ru/$Mg_{(1-X)}Zn_XO$ catalysts synthesis

The catalyst was prepared by excessive impregnation method. First, the prepared Ba–$Mg_{(1-X)}Zn_XO$ and $Mg_{(1-X)}Zn_XO$ were impregnated with $Ru_3(CO)_{12}$ in a certain amount of tetrahydrofuran solution, while being continuously stirred at room temperature for 12 h. The mixture was dried in a water bath at 50 °C, followed dried in a drying oven at 60 °C. Then it was decomposed in a vacuum of 450 °C for 3 h, after which it was cooled down to room temperature under an atmosphere of H_2. Finally, it was pressed, crushed and screened to obtain catalyst with a Ru loading capacity of 2 wt%.

2.4 Catalytic performance test

The catalytic activity of the prepared catalyst for ammonia synthesis was evaluated in a fixed bed flow reactor containing 0.5 mL of catalyst. Prior to the test, the catalyst was heated in a gas mixture of 25%N_2–75%H_2 from 400 °C to 500 °C, with a temperature gradient of 25 °C activated for 2 h at each temperature, and the heating rate was 10 °C min^{-1}. This step aimed to reduce Ru and Ba species. Then, the temperature was decreased to 425 °C, 400 °C and 375 °C, respectively, and the reaction rate was evaluated at each temperature. The test conditions were 18 000 h^{-1}, 0.2 MPa and $H_2 : N_2 = 3 : 1$. The performance data for each catalyst was tested triplicate and averaged.

3. Results and discussions

3.1 Catalytic performance

A comprehensive evaluation of Ru/Ba–$Mg_{(1-X)}Zn_XO$ ($0.10 > X > 0$) catalysts for ammonia synthesis performance was shown in Fig. 1a. Under test conditions of 18 000 h^{-1}, 0.2 MPa and 400 °C, the Ru/Ba–MgO catalyst has an ammonia synthesis rate of 1.11 mmol g^{-1} h^{-1}. Introduction of Zn doping resulted in a significant enhancement of the ammonia synthesis rate for the Ru/Ba–$Mg_{0.97}Zn_{0.03}O$ catalyst, reaching 1.73 mmol g^{-1} h^{-1}. This observation indicates an optimal Zn doping level was beneficial for enhancing ammonia synthesis activity. However, as X increased from 0.03 to 0.10, the ammonia synthesis rate of the catalyst decreased to 1.38 mmol g^{-1} h^{-1}, indicating that excessive Zn doping would inhibit ammonia synthesis. Concurrently, the activation energy of the Ru/Ba–$Mg_{(1-X)}Zn_XO$ catalysts was fitted by Arrhenius equation and shown in Fig. 1b. Over the temperature range was 425 °C to 375 °C, the activation energy (E_a) value of Ru/Ba–$Mg_{(1-X)}Zn_XO$ catalysts initially decreased and then increased, reaching the minimum of 65.35 kJ mol^{-1} when $X = 0.03$. This indicates that the Zn addition accelerated the reaction rate of H_2 and N_2 on Ru/MgO catalyst.

3.2 Structural characterizations of the catalysts

The crystal structure of the Ru/Ba–$Mg_{(1-X)}Zn_XO$ catalyst was characterized by XRD. As shown in Fig. 2a, the Bragg diffraction peaks at 2θ values of 36.7°, 42.7°, 62.1°, 74.5°, and 78.4° corresponded to the (111), (200), (220), (311), and (222) crystal planes of the MgO, respectively. Because MgO support possesses *Fm*3*m* space group with a face-centered cubic (fcc) structure (PDF#04-009-5446). The high crystallinity of the MgO support was evident from the sharp Bragg diffraction peaks observed in the Ru/Ba–MgO catalyst. And no significant changes were observed in the Bragg diffraction peak of the Zn-doped Ru/Ba–$Mg_{(1-X)}Zn_XO$ catalyst. However, no ZnO phases were present. Upon increasing the value of X to 0.3, the phase of ZnO (PDF#04-001-7297) with wurtzite structure appeared in the sample, indicating the formation of $Mg_{(1-X)}Zn_XO$ solid solution at X below 0.3 (Fig. S1†). Given that the ionic radius of Zn^{2+} (0.074 Å) is slightly larger than that Mg^{2+} (0.072 Å), Zn^{2+} incorporation into the MgO lattice leads to an increase in lattice spacing. This was evident from the enlarged Bragg diffraction profile of MgO (200) crystal plane in Fig. 2a, where a shift in the Bragg diffraction peak was observed upon Zn doping. Furthermore, the HRTEM images in Fig. 2b and c showed that the substitution of Mg^{2+} by Zn^{2+} resulted in an expanded lattice

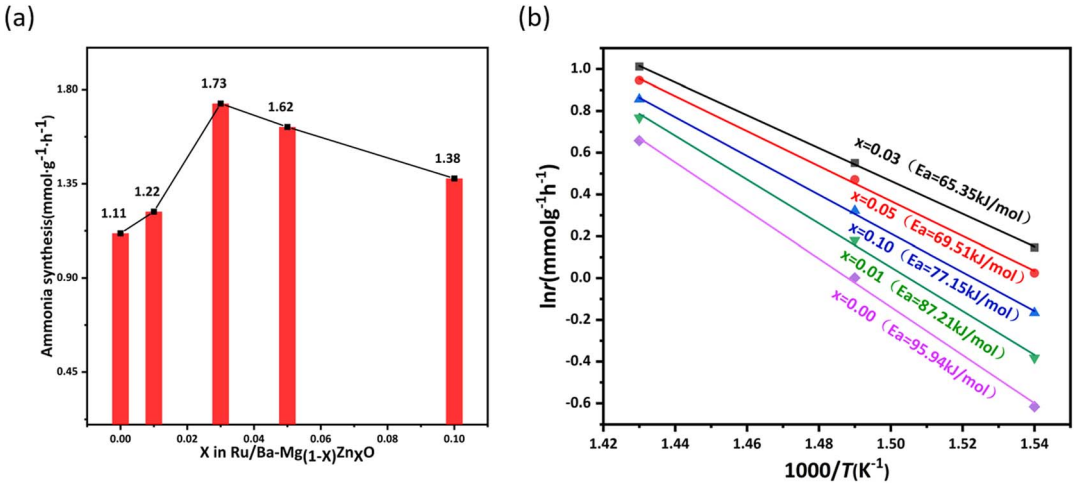

Fig. 1 (a) Ammonia synthesis rate of Ru/Ba–$Mg_{(1-X)}Zn_XO$ catalysts. Test condition: 0.2 MPa, 400 °C, 18 000 h^{-1}. (b) E_a of Ru/Ba–$Mg_{(1-X)}Zn_XO$ catalysts (375–425 °C).

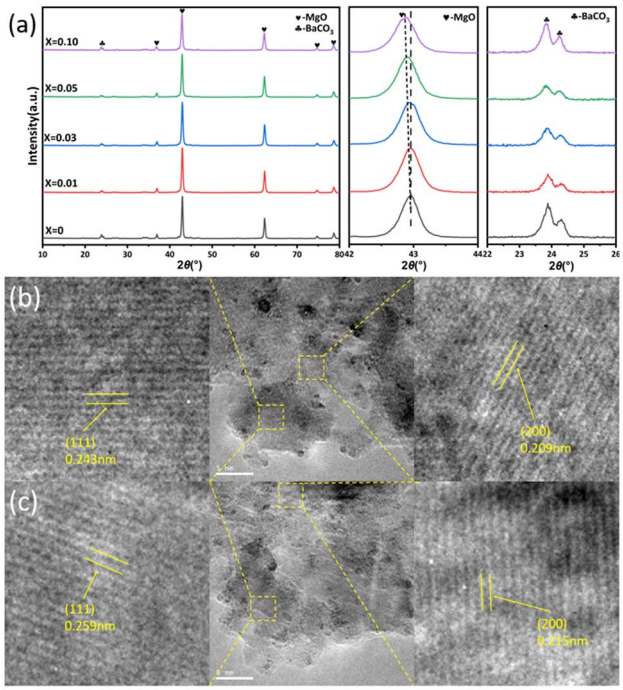

Fig. 2 (a) XRD results of Ru/Ba–$Mg_{(1-X)}Zn_XO$ catalysts and amplification of the position at 42–44° and 22–26° of 2θ angle. (b) Lattice spacing of the (200) and (111) crystal planes of Ru/Ba–MgO (c) lattice spacing of the (200) and (111) crystal planes of Ru/Ba–$Mg_{0.97}Zn_{0.03}O$ catalysts.

spacing, with the (111) and (200) crystal planes of MgO increasing from 0.243 nm and 0.209 nm (Ru/Ba–MgO) to 0.259 nm and 0.215 nm (Ru/Ba–$Mg_{0.97}Zn_{0.03}O$), respectively. Collectively, these results confirmed the substitution of Mg^{2+} by Zn^{2+} to form a solid solution structure.

The microscopic surface structure and morphology were characterized by SEM and N_2-TPD. The Ba–$Mg_{(1-X)}Zn_XO$ supports exhibited an irregular nanoparticle shape (Fig. 3a–e). When $X = 0$, 0.01 and 0.03, there was no significant change in particle size, ranging from 40–60 nm. However, at $X = 0.05$ and 0.10, a slight increase in the support was observed. This indicated that Zn doping could influence the particle size of the support, but the effect was less pronounced at lower Zn content. The grain sizes calculated by Williamson–Hall formula, were listed in Table S1.† It was observed that the trend in grain size change was not particularly evident, except for a notable increase to 35.2 nm at $X = 0.10$. This slight alteration in grain size indicated a weak influence of Zn micro-doping on the support particles. The N_2-TPD curves of the Ba–$Mg_{(1-X)}Zn_XO$ supports uniformly exhibited type IV characteristics, featuring a distinct H4-type hysteresis loop at higher relative pressures (P/P_0 = 0.9∼1.0). This observation indicated the presence of mesoporous structures in all modified supports (Fig. S2a†). The pore size distribution plot of Fig. S2a† showed two primary pore sizes: approximately 7 nm mesopores and approximately 60 nm macropores, respectively. The micropores were attributed to the internal pores of the supports, while the size of the macropores was close to that of the support particles, possibly due to particle accumulation. With the increase of X, the average pore size decreased, reflecting an increase in the number of mesopores. Conversely, the number of macropores decreased, leading to an increase in pore size (Table S1†). Furthermore, the pore volume generally increased with X (Table S1†). At the same time, the specific surface area (S_{BET}) of the supports obtained by BET method remained relatively consistent for X values of 0, 0.01 and 0.03. However, as X increased to 0.05 and 0.1, the S_{BET} reached ∼130 $m^2\ g^{-1}$, showing a general upward trend (Table S1†). This trend was similar to that of catalyst morphology. Nevertheless, as showed in Fig. 1a, the S_{BET}, pore and morphology were not the primary determinants of the catalytic performance, and no discernible correlation was observed between them.

The size of Ru NPs has a significant effect on the activity of Ru-based ammonia synthesis catalysts. The B5 site, which is the active site for the Ru in Ru based ammonia synthesis

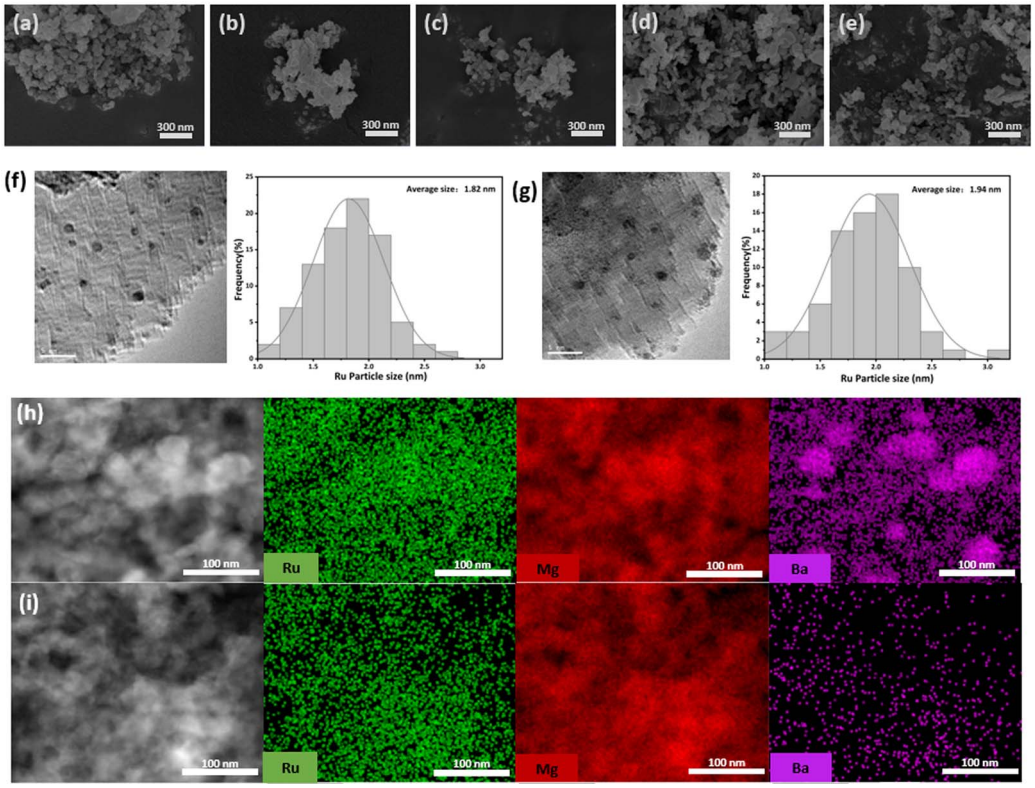

Fig. 3 SEM of Ru/Ba–$Mg_{(1-X)}Zn_XO$ catalysts (a) $X = 0$ (b) $X = 0.01$ (c) $X = 0.03$ (d) $X = 0.05$ (e) $X = 0.10$. (f) Size distribution of Ru nanoparticles in Ru/Ba–MgO catalyst. (g) Size distribution of Ru nanoparticles in Ru/Ba–$Mg_{0.97}Zn_{0.03}O$ catalyst. (h) TEM-Mapping of Ru/Ba–MgO catalyst. (i) TEM-Mapping of Ru/Ba–$Mg_{0.97}Zn_{0.03}O$ catalyst.

catalysts,[36,37] is primarily influenced by the size of Ru NPs. Notably, and Ru nanoparticles within the range of 1.8–2.5 nm have the highest concentration of B5 active site.[38] Therefore, we focused on examining the influence of Zn doping on the size of Ru NPs in Ru/Ba–MgO and Ru/Ba–$Mg_{0.97}Zn_{0.03}O$ catalysts. The average sizes of Ru NPs in both catalysts were obtained by TEM and particle size statistics software (Fig. 3f and g). The average size of the Ru NPs of the Ru/Ba–MgO and Ru/Ba–$Mg_{0.97}Zn_{0.03}O$ catalysts was 1.82 nm and 1.94 nm, respectively. Both sizes fell within the optimal range of 1.8–2.5 nm. It was found that the doping of Zn did not significantly change the size of Ru NPs. This may be due to the fact that both supports possessed sufficient specific surface areas for effective for Ru dispersion, and the average pore size did not reach *a* point where it impacted the dispersion of the Ru nanoparticles. Nevertheless, while the size of Ru NPs was very important, it was not the *s* determinant of catalytic activity for Ru/Ba–$Mg_{(1-X)}Zn_XO$ catalysts.

Alkali metal or alkaline earth metal auxiliaries play an important role in increasing the ammonia synthesis rate.[39] For Ru-based catalysts, amorphous Ba was more beneficial for ammonia synthesis reaction.[40] Recent studies have suggested that this may be attributed to the formation of the Ba–Ru interface through the highly dispersed Ba in proximity to Ru NPs.[41] Therefore, it was imperative to achieve higher dispersibility of Ba. The EDS results of the catalyst were shown in Table S2.† In Ru/Ba–$Mg_{(1-X)}Zn_XO$ catalysts, the Ba content was relatively similar. Therefore, the content of additive Ba had *q* limited impact on the performance of catalyst. However, when $X = 0$, Ba had the sharpest Bragg diffraction peak, and the content of Ba was 1.93 wt%. In contrast, when $X = 0.03$, the sharpness of Ba Bragg diffraction peak decreased significantly, and the content of Ba reached its highest value of 2.68 wt% (Fig. 1). This indicated that the optimal level of Zn doping slightly facilitates the incorporation of Ba on the support but significantly promoted its dispersion. However, TEM-Mapping showed that the distribution of Ba in the Ru/Ba–$Mg_{0.97}Zn_{0.03}O$ catalyst was significantly more dispersed, with almost no lumpy Ba, compared to the Ru/Ba–MgO (Fig. 3h and i). Additionally, Fig. S3† showed the H_2-TPD curves of Ru/Ba–$Mg_{0.97}Zn_{0.03}O$ and Ru/Ba–MgO catalysts, and the hydrogen desorption peak at 350–600 °C was attributed to the adsorption of hydrogen by Ru.[42] The desorption peak at 700–800 °C of Ru/Ba–$Mg_{0.97}Zn_{0.03}O$ catalyst was attributed to the adsorption of hydrogen by Ba, when Ru and highly dispersed Ba form Ru–Ba interfaces.[41] The peak area of Ru/Ba–$Mg_{0.97}Zn_{0.03}O$ catalyst was higher than that of Ru/Ba–MgO catalyst, indicating that the majority of the highly dispersed Ba in Ru/Ba–$Mg_{0.97}Zn_{0.03}O$ catalyst was in close contact with Ru, promoting the formation of Ba–Ru interfaces. In contrast, in Ru/Ba–MgO catalysts, only a fraction of Ba was dispersed and was in contact with Ru. The results of H_2-TPD and TEM proved that Zn doping promoted Ba

dispersion. Furthermore, the sharpness of Ba's Bragg diffraction peak proved this observation, as shown the enlarged section in Fig. 1. Therefore, the improved catalyst performance was attributed to the change in Ba morphology from bulk to amorphous.

In order to further elucidate the impact of Zn doping on catalyst support, electron paramagnetic resonance (EPR) was used to demonstrate the enhancement of OVs formation due to Zn doping. As shown in Fig. 4a, both Ru/MgO and Ru/$Mg_{0.97}Zn_{0.03}O$ catalysts had a symmetric EPR signal peak at $g =$ 2.003. This peak was attributed to unpaired electrons at the OVs point of the nanomaterials.[43] It could be seen that the Zn doping was enhanced EPR signal, indicating that the Zn doping promoted the formation of OVs.

Further, DFT calculation confirmed that Zn doping promoted the generation of OVs in MgO. And the Mg^{2+} substitution energy (E_{sub}) was calculated for various crystal planes (Table S3†). Specifically, the E_{sub} value for Mg^{2+} in MgO (200) crystal plane was 322 kJ mol^{-1}, while it was only 58.1 kJ mol^{-1} in MgO (111) crystal plane (Fig. 4b). This finding indicated that Zn^{2+} was more likely to displace Mg^{2+} on the (111) crystal plane of MgO. Additionally, the oxygen vacancy formation energy (E_{OV}) was calculated both before and after Zn doping (Fig. S4, S5 and Table S4†). The E_{OV} of the (200) crystal plane was 6.29 eV, in contrast to only 2.98 eV for the (111) crystal plane (Fig. 4c and d). A comparison of the E_{OV} values before and after Zn doping showed that Zn doping significantly reduced the E_{OV}. Specifically, the E_{OV} of the (200) crystal plane decreased by 0.73 eV (from 6.29 eV to 5.56 eV), while the E_{OV} of the (111) crystal plane decreased by 0.12 eV (from 2.98 eV to 2.86 eV). The above results indicated that Zn^{2+} prefers to replace Mg^{2+} at the (111) crystal plane, thereby promoting the formation of OVs at this plane. The results were corroborated with EPR.

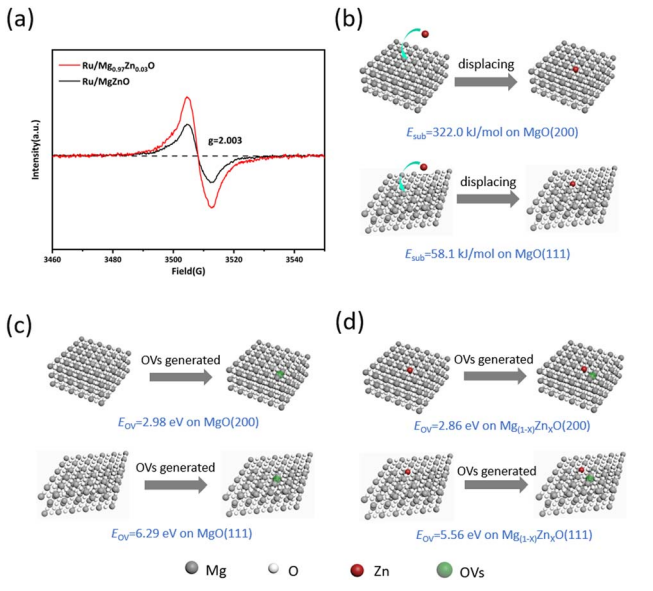

Fig. 4 (a) EPR spectrums of Ru/$Mg_{(1-X)}Zn_XO$ and Ru/MgO catalysts (b) substitution energy (E_{sub}) on different crystal faces of MgO. (c) Oxygen vacancy formation energy (E_{OV}) before Zn doping on (200) and (111) crystal planes of MgO. (d) Oxygen vacancy formation energy (E_{OV}) after Zn doping on (200) and (111) crystal planes of $Mg_{(1-X)}Zn_XO$.

3.3 Oxygen vacancies anchored and dispersed Ba

The relationship between OVs and Ba dispersion in Ru/Ba–$Mg_{(1-X)}Zn_XO$ catalysts was studied by XPS. In order to investigate the influence of OVs on Ba, Ru/Ba–$Mg_{(1-X)}Zn_XO$ and Ru/$Mg_{(1-X)}Zn_XO$ catalysts were prepared for analysing OVs in the presence and absence of Ba. The O 1s XPS spectrum of the Ru/$Mg_{(1-X)}Zn_XO$ ($0.10 > X > 0$), shown in Fig. 5a, was used to verify OVs generation. This spectrum could be deconvoluted into three peaks, attributed to surface adsorbed oxygen (M-OH), OVs, and lattice oxygen (LO), respectively.[44–46] By studying the trend, it was observed that with the increase of X, the OVs content initially increased, then decreased, and finally increased again. And the OVs content reached its maximum at $X = 0.03$. Specifically, When $X = 0$, OVs content in MgO was 25.20%, and when $X = 0.03$, the OVs content significantly increased to 35.12%. Fig. 5b showed the O 1s XPS spectra of the Ru/Ba–$Mg_{(1-X)}Zn_XO$ catalysts. Since Ba existed on the surface of Ru/Ba–MgZnO as bulks of $BaCO_3$, it generates a strong CO_3^{2-} signal, which overlays the lattice oxygen (LO) signal (Fig. 3h). Moreover, the XPS peak position of the O atom in CO_3^{2-} closely aligns with that of the OVs.[47] Therefore, the O 1s XPS spectrum of Ru/Ba–$Mg_{(1-X)}Zn_XO$ was deconvolved into four peaks, and the peak trends were analyzed. With the increase of X, the content of OVs in the Ru/Ba–$Mg_{(1-X)}Zn_XO$ catalysts showed a trend of decreasing followed by an increase, reaching a minimum of 12.7% at $X = 0.03$. This result was opposite to the trend of OVs content in Ru/$Mg_{(1-X)}Zn_XO$ without Ba (Fig. 5a). This was due to the generation of numerous OVs upon Zn doping, and this OVs served as anchored points for Ba, facilitating its dispersion from a large-sized bulk to a highly dispersed morphology. However, the OVs as anchor points could not be characterized by XPS due to their coverage by Ba (Fig. 6). The increased anchoring of Ba by OVs resulted in a decrease in the number of detectable OVs, leading to a corresponding decrease in their detection. Analysis of the O 1s XPS spectrum for both the Ru/$Mg_{(1-X)}Zn_XO$ ($0.10 > X > 0$) and Ru/Ba–$Mg_{(1-X)}Zn_XO$ indicated a positive correlation between OVs content and Ba anchoring, resulting in improved Ba dispersion. This was consistent with the Ba dispersion obtained by Mapping, H_2-TPD and XRD.

Further, with the increase of X, the OVs peaks of Ru/Ba–$Mg_{(1-X)}Zn_XO$ catalysts showed a distinct trend of initially shifting towards the high binding energy direction, followed by a shift towards the low binding energy direction, which was opposite to the Ru/$Mg_{(1-X)}Zn_XO$ catalysts (Fig. 5a and b). In general, the magnitude of the electron binding energy reflects the electron density of that metal. The lower the binding energy, the higher the electron density of the surface metal.[48] The Ba $3d_{5/2}$ XPS peak of Ru/Ba–$Mg_{(1-X)}Zn_XO$ catalyst had a consistent trend with O 1s XPS peak, while it was opposite to that of Ru $3d_{5/2}$ XPS peak (Fig. 5c and d). This was due to the close contact formed by OVs, Ba, and Ru. In this configuration, electrons from Ba and OVs were transferred to Ru, leading to an increase

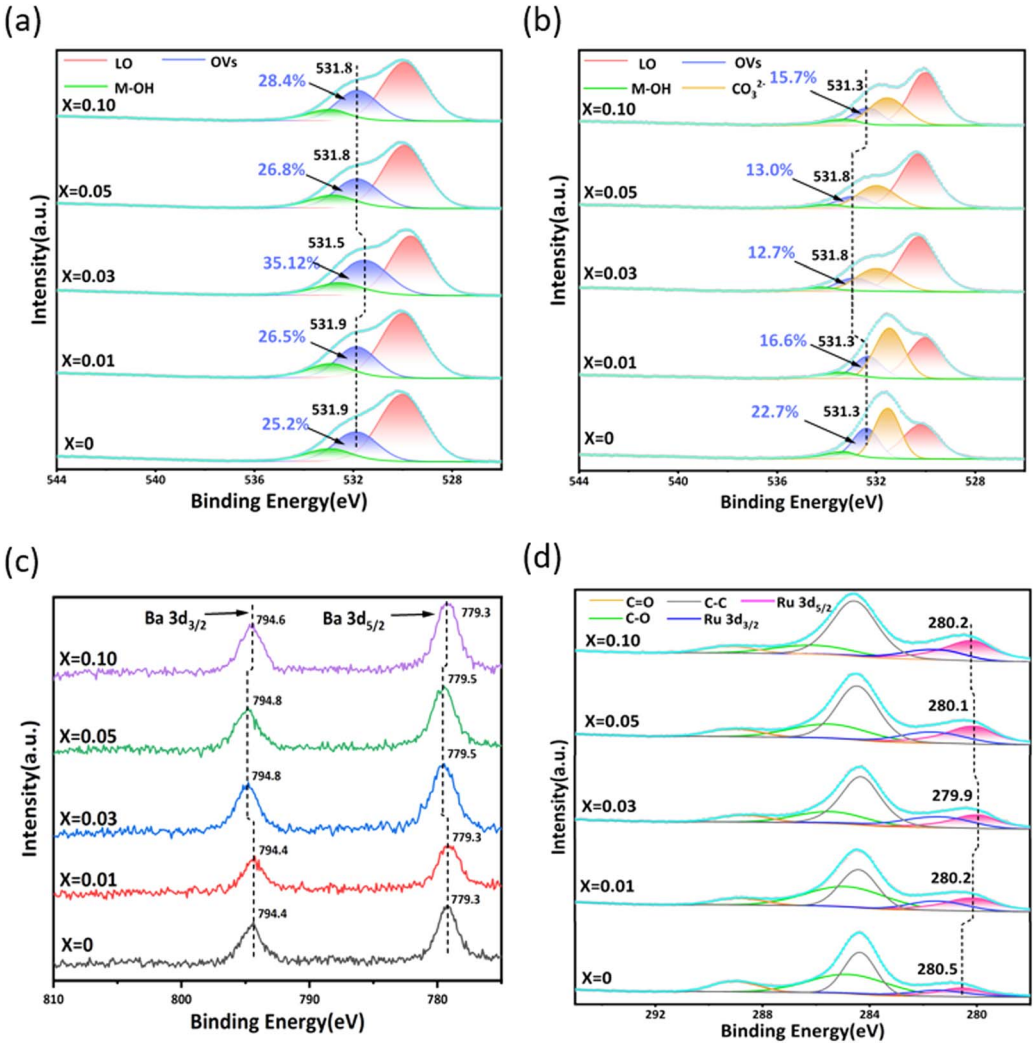

Fig. 5 (a) O 1s XPS spectrums of Ru/Ba–MgZnO catalysts and its deconvolution results. (b) O 1s XPS spectrums of Ru/Ba–$Mg_{(1-X)}Zn_XO$ catalysts and its deconvolution results. (c) Ba $3d_{3/2}$ and $3d_{5/2}$ XPS spectrums of Ru/Ba–$Mg_{(1-X)}Zn_XO$ catalysts. (d) Ru 3d XPS spectrums of Ru/Ba–$Mg_{(1-X)}Zn_XO$ catalysts and its deconvolution results.

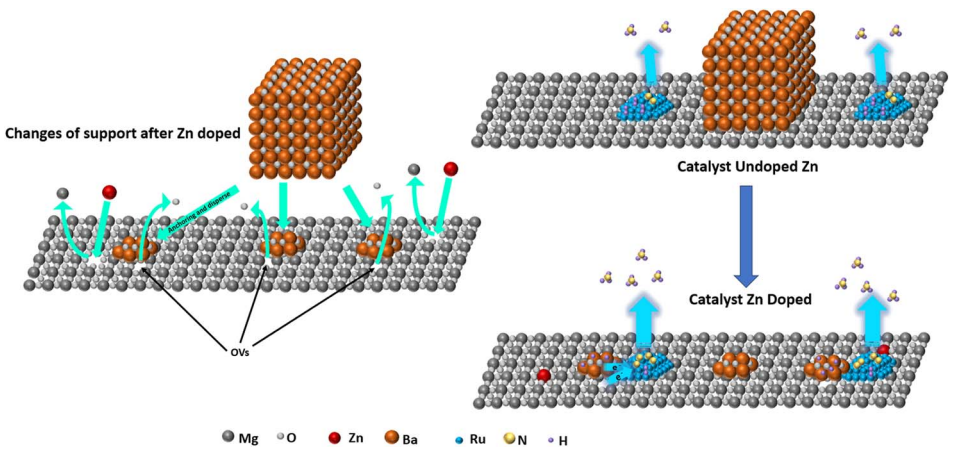

Fig. 6 The oxygen vacancy generated by atom doping was used to anchor and disperse the promoter Ba on the MgO support to improve ammonia synthesis activity.

in the electron density on Ru's surface. Electrons on the OVs were more apt to be transferred to Ru *via* Ba than directly. For the active component Ru, the increase of its electron density facilitates its ability to dissociate and adsorb N_2.

3.4 Kinetics experiment

To investigate the impact of Ba morphology and support OVs on ammonia synthesis, the reaction orders of N_2, H_2, and NH_3 were studied for Ru/MgO, Ru/Ba–MgO, Ru/$Mg_{0.97}Zn_{0.03}O$ and Ru/Ba–$Mg_{0.97}Zn_{0.03}O$ catalysts (Fig. 7a, b and S6†). Specifically, the Reaction orders of H_2 and N_2 for Ru/MgO and Ru/$Mg_{0.97}Zn_{0.03}O$ catalysts were compared to assess the influence of OVs on catalytic performance. The reaction order of N_2 increased from 0.46 to 0.53, while that of H_2 rose from −0.45 to −0.41. This indicated that oxygen vacancy can promote the dissociative adsorption of nitrogen and hydrogen, which was attributed to the adsorption of hydrogen onto oxygen vacancy, thereby mitigating hydrogen poisoning.[31,32] However, the OVs seem to be detrimental to ammonia decomposition. By comparing the reaction orders of Ru/$Mg_{0.97}Zn_{0.03}O$ and Ru/Ba–$Mg_{0.97}Zn_{0.03}O$ catalysts, it could be seen that the H_2 reaction order of Ru/Ba–$Mg_{0.97}Zn_{0.03}O$ catalyst was 0.08, higher than that of Ru/Ba–MgO catalyst, and the N_2 reaction order of Ru/Ba–$Mg_{0.97}Zn_{0.03}O$ catalyst was higher. This was attributed to the fact that dispersed Ba could adsorb H_2, compared to agglomerated Ba, reducing the competitive adsorption of H_2 and N_2 on Ru.[41] In summary, OVs did have the capacity to inhibit hydrogen poisoning, but this capacity was weaker than Ba. The mechanism of inhibiting hydrogen poisoning by Zn doping was elucidated by kinetic experiments. The transformation of the aggregated Ba into a highly dispersed state by OVs was the primary reason for inhibiting hydrogen poisoning in the Ru/Ba–$Mg_{0.97}Zn_{0.03}O$ catalyst.

3.5 Surface acid-alkalinity and MSI

Fig. 8 showed the CO_2-TPD results of Ru/Ba–$Mg_{(1-X)}Zn_XO$ catalysts. The analysis of all the CO_2-TPD curves of the catalysts could be divided into two distinct CO_2 desorption zones: the weakly basic adsorption site (α) at 50–200 °C and the moderately basic adsorption site (β) at 200–500 °C. These zones may be related to the two basic sites of OH^- and metal–oxygen pairs, respectively.[49] The peak areas of the two CO_2 desorption peaks were calculated and shown in Table S5.† It is noteworthy that the peak areas for the weakly basic sites (α) remained relatively constant with increasing Zn doping (X). In contrast, the peak areas for the moderately basic sites (β) exhibited significant variations. In comparison to the undoped catalysts, the Zn-doped catalysts exhibited an increase in peak areas for the weakly basic sites, following a trend of initial increase followed by a decrease. On the other hand, the peak areas of the moderately basic sites showed more substantial changes, albeit without a discernible pattern. Overall, in the Ru/Ba–$Mg_{(1-X)}Zn_XO$ catalysts, as the Zn doping amount increases, the basicity first decreased, then increased and finally gradually decreased. When the Zn doping amount was 0.03, the Ru/Ba–$Mg_{(1-X)}Zn_XO$ catalysts had the maximum basicity density which was beneficial for the catalytic reaction. CO_2-TPD results showed that the moderate doping of Zn could promote the generation of more basic sites on the Ru/Ba–$Mg_{(1-X)}Zn_XO$ catalysts, with stronger

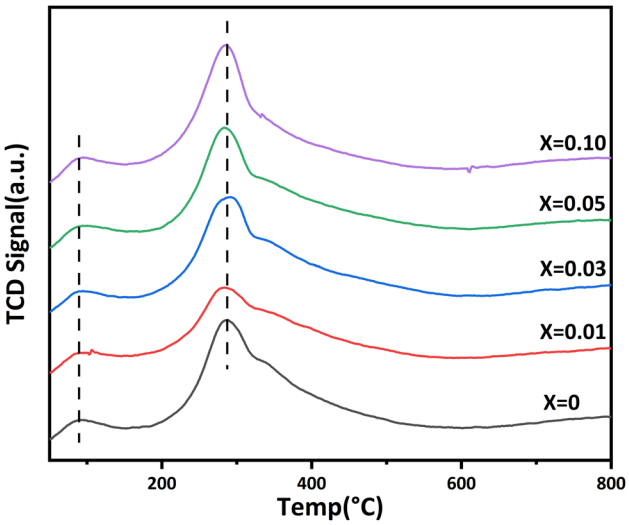

Fig. 8 CO_2-TPD curve of Ru/Ba–$Mg_{(1-X)}Zn_XO$ catalysts.

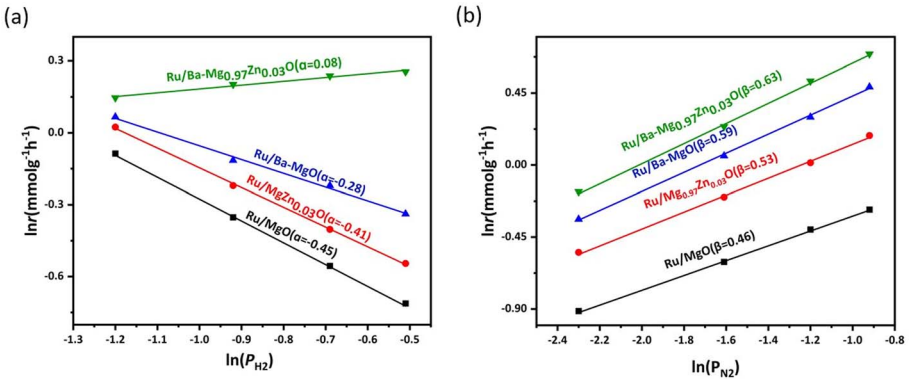

Fig. 7 (a) Reaction orders of H_2 for Ru/MgO, Ru/Ba–MgO, Ru/$Mg_{0.97}Zn_{0.03}O$ and Ru/Ba–$Mg_{0.97}Zn_{0.03}O$ catalysts. (b) Reaction orders of N_2 for Ru/MgO, Ru/Ba–MgO, Ru/$Mg_{0.97}Zn_{0.03}O$ and Ru/Ba–$Mg_{0.97}Zn_{0.03}O$ catalysts.

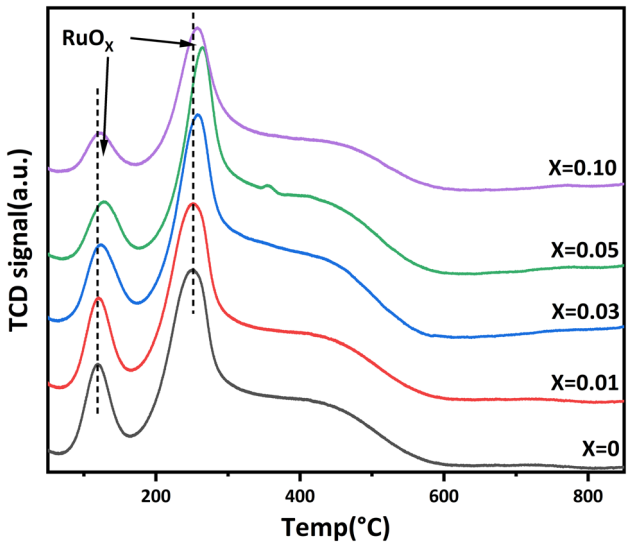

Fig. 9 H_2-TPR curves of Ru/Ba–$Mg_{(1-X)}Zn_XO$ catalysts.

electron-donating ability. This could help generate highly active electron-rich ruthenium, thereby improving its ammonia synthesis reaction activity.[50,51]

The metal-support interaction was closely related to the activity of the catalyst.[52] Therefore, the reduction performance of Ru/Ba–$Mg_{(1-X)}Zn_XO$ catalysts was investigated by H_2-TPR, and the results were shown in Fig. 9. Three distinct hydrogen-consuming peaks appeared in H_2-TPR curves, located at 50–150 °C, 200–300 °C and 400–500 °C, respectively. The hydrogen-consumption peaks at 50–150 °C and 200–300 °C were attributed to the two-stage reduction of Ru oxygen species (RuO_X) in the catalyst,[53,54] which was observed not only in MgO supports but also in Ru-based catalysts with cerium dioxide as the support. These peaks represent the strong and weak interactions of RuO_X with the support, respectively.[55] The peak at 400–500 °C was attributed to the low-temperature decomposition of $BaCO_3$ (LT-$BaCO_3$).[56] The peak temperature of RuO_X shifted initially to high-temperature direction, and then gradually to the low-temperature direction with increasing *X*. This change may be influenced by the OVs on the surface of the support. It is hypothesized that the microcosmic surface complexity of the support increased due to the surface defect of OVs, subsequently enhancing the metal-support interaction.

4. Conclusion

In this study, Zn atom doping was employed to modify Ru/Ba–MgO catalyst support. Our findings indicated that a minor amount of Zn doping did not significantly alter the support surface morphology, surface texture and the dispersion of the active Ru component. However, Zn doping did promote the increase of OVs content in the support. This elevated OVs content effectively inhibited the aggregation of Ba, serving as anchor points for Ba promoter. This led to promote the dispersion of Ba, formation of additional Ba–Ru interfaces, and mitigation of hydrogen poisoning in the catalyst. Concurrently, the dispersed Ba also promoted electron transfer to the active Ru component, increasing its electron density of Ru, and significantly improving the performance of the Zn-doped MgO supported Ru-based ammonia synthesis catalyst.

Author contributions

Yuanjie Chen: writing original draft, conceptualization, formal analysis Junqiao He: methodology, writing original draft Haiyan Lei: methodology, Qunyao Tu: data curation Chen Huang: visualization Xiangwei Cheng: writing review & editing Xiazhen Yang: validation Huazhang Liu: supervision Chao Huo: writing review & editing, funding acquisition.

Conflicts of interest

The authors declare that they have no known competing financial interests or personal relationships that could have appeared to influence the work reported in this paper.

Acknowledgements

The authors are grateful to the Natural Science Foundation of Zhejiang Province (LY18B060015, LQ19B060007) and Research project Foundation of Zhejiang University of Technology (KYY-HX-20240030). And the authors would like to acknowledge Prof. Riguang. Zhang from the Institute of Coal Chemistry, Taiyuan University of Technology, for his support in DFT calculations.

References

1 H. Liu, W. Han, C. Huo and Y. Cen, Development and application of wustite-based ammonia synthesis catalysts, *Catal. Today*, 2020, **355**, 110–127, DOI: 10.1016/j.cattod.2019.10.031.
2 H. Fang, D. Liu, Y. Luo, Y. Zhou, S. Liang, X. Wang, B. Lin and L. Jiang, Challenges and Opportunities of Ru-Based Catalysts toward the Synthesis and Utilization of Ammonia, *ACS Catal.*, 2022, **12**(7), 3938–3954, DOI: 10.1021/acscatal.2c00090.
3 C. Zamfirescu and I. Dincer, Ammonia as a green fuel and hydrogen source for vehicular applications, *Fuel Process. Technol.*, 2009, **90**(5), 729–737, DOI: 10.1016/j.fuproc.2009.02.004.
4 J. G. Chen, R. M. Crooks, L. C. Seefeldt, K. L. Bren, R. M. Bullock, M. Y. Darensbourg, P. L. Holland, B. Hoffman, M. J. Janik, A. K. Jones, M. G. Kanatzidis, P. King, K. M. Lancaster, S. V. Lymar, P. Pfromm, W. F. Schneider and R. R. Schrock, Beyond fossil fuel-driven nitrogen transformations, *Science*, 2018, **360**, 6391, DOI: 10.1126/science.aar6611.
5 I. Rossetti, N. Pernicone and L. Forni, Graphitised carbon as support for Ru/C ammonia synthesis catalyst, *Catal. Today*, 2005, **82**(8–9), 725–727, DOI: 10.1016/j.cattod.2005.02.010.
6 B. Lin, Y. Guo, C. Cao, J. Ni, J. Lin and L. Jiang, Carbon support surface effects in the catalytic performance of Ba-

promoted Ru catalyst for ammonia synthesis, *Catal. Today*, 2018, **316**, 230–236, DOI: 10.1016/j.cattod.2018.01.008.

7 A. Jafari, N. Saadatjou and S. Sahebdelfar, Influence of chemical treatments of activated carbon support on the performance and deactivation behavior of promoted Ru catalyst in ammonia synthesis, *Int. J. Hydrogen Energy*, 2015, **40**(9), 3659–3671, DOI: 10.1016/j.ijhydene.2015.01.071.

8 H. Bielawa, O. Hinrichsen, A. Birkner and M. Muhler, The Ammonia-Synthesis Catalyst of the Next Generation: Barium-Promoted Oxide-Supported Ruthenium, *Angew. Chem., Int. Ed.*, 2001, **40**(6), 1061–1063, DOI: 10.1002/1521-3773(20010316)40:6<1061::AID-ANIE10610>3.0.CO;2-B.

9 J. Ni, S. Shi, C. Zhang, B. Fang, X. Wang, J. Lin, S. Liang, B. Lin and L. Jiang, Enhanced catalytic performance of the carbon-supported Ru ammonia synthesis catalyst by an introduction of oxygen functional groups via gas-phase oxidation, *J. Catal.*, 2022, **49**, 78–86, DOI: 10.1016/j.jcat.2022.03.026.

10 C. J. H. Jacobsen, Novel class of ammonia synthesis catalysts, *Chem. Commun.*, 2000, **12**(12), 1057–1058, DOI: 10.1039/b002930k.

11 T.-N. Ye, S.-W. Park, Y. Lu, J. Li, M. Sasase, M. Kitano, T. Tada and H. Hosono, Vacancy-enabled N_2 activation for ammonia synthesis on an Ni-loaded catalyst, *Nature*, 2020, **583**(7816), 391–395, DOI: 10.1038/s41586-020-2464-9.

12 J. Huang, M. Yuan, X. Li, Y. Wang, M. Li, J. Li and Z. You, Cs-Promoted ruthenium catalyst supported on $Ba_5Ta_4O_{15}$ with abundant oxygen vacancies for ammonia synthesis, *Appl. Catal., A*, 2021, **615**, 118058, DOI: 10.1016/j.apcata.2021.118058.

13 N. Masayasu, C. Shih-Yuan, T. Hiroyuki, M. Takehisa, T. Hideyuki and N. Tetsuya, A super-growth carbon nanotubes-supported, Cs-promoted Ru catalyst for 0.1–8 MPaG ammonia synthesis, *J. Catal.*, 2022, **413**, 623–635, DOI: 10.1016/j.jcat.2022.07.015.

14 C. Shih-Yuan, W. Li-Yu, C. Kai-Chun, Y. Cheng-Hsi, H. Wei-Chih, C. Hsin-Yu, N. Masayasu, K. Martin, C. Chih-Li, L. Chien-Neng, M. Takehisa, C. Hsin-Yi Tiffany, C. Ho-Hsiu and Y. Chia-Min, Ammonia synthesis over cesium-promoted mesoporous-carbon-supported ruthenium catalysts: Impact of graphitization degree of the carbon support, *Appl. Catal., B*, 2024, **346**, 123725, DOI: 10.1016/j.apcatb.2024.123725.

15 J. Feng, X. Zhang, J. Wang, X. Ju, L. Liu and P. Chen, Applications of rare earth oxides in catalytic ammonia synthesis and decomposition, *Catal. Sci. Technol.*, 2021, **11**(19), 6330–6343, DOI: 10.1039/d1cy01156a.

16 R. Javaid and T. Nanba, Effect of texture and physical properties of catalysts on ammonia synthesis, *Catal. Today*, 2021, **397**, 592–597, DOI: 10.1016/j.cattod.2021.06.007.

17 S. E. Siporin and R. J. Davis, Isotopic transient analysis of ammonia synthesis over Ru/MgO catalysts promoted by cesium, barium, or lanthanum, *J. Catal.*, 2004, **222**(2), 315–322, DOI: 10.1016/j.jcat.2003.10.018.

18 H. Ronduda, M. Zybert, W. Patkowski, A. Ostrowski, P. Jodlowski, D. Szymanski, L. Kepinski and W. Rarog-Pilecka, A high performance barium-promoted cobalt catalyst supported on magnesium-lanthanum mixed oxide for ammonia synthesis, *RSC Adv.*, 2021, **11**(23), 14218–14228, DOI: 10.1039/d1ra01584b.

19 H. Bielawa, O. Hinrichsen, A. Birkner and M. Muhler, The ammonia-synthesis catalyst of the next generation: Barium-promoted oxide-supported ruthenium, *Angew. Chem., Int. Ed.*, 2001, **40**(6), 1061–1063, DOI: 10.1002/1521-3773(20010316)40:6<1061::AID-ANIE10610>3.0.CO;2-B.

20 X. Yang, L. Tang, C. Xia, X. Xiong, X. Mu and B. Hu, Effect of MgO/h-BN Composite Support on Catalytic Activity of Ba-Ru/MgO/h-BN for Ammonia Synthesis, *Chin. J. Catal.*, 2012, **33**(3), 447–453, DOI: 10.1016/S1872-2067(11)60352-5.

21 M. Moulavi, K. Kanade, D. Amalnerkar, A. Fatehmulla, A. M. Aldhafiri and M. Aslam Manthrammel, Synergistic surface basicity enhancement effect for doping of transition metals in nanocrystalline MgO as catalysts towards one pot Wittig reaction, *Arabian J. Chem.*, 2021, **14**(5), 103134, DOI: 10.1016/j.arabjc.2021.103134.

22 C. Wildfire, V. Abdelsayed, D. Shekhawat, R. A. Dagle, S. D. Davidson and J. Hu, Microwave-assisted ammonia synthesis over Ru/MgO catalysts at ambient pressure, *Catal. Today*, 2020, **365**, 103–110, DOI: 10.1016/j.cattod.2020.06.013.

23 W. Li, Y. Ye, S. Zhang, C. Liang and H. Zhang, A fluidized electrocatalysis approach for ammonia synthesis using oxygen vacancy-rich Co_3O_4 nanoparticles, *Inorg. Chem. Front.*, 2021, **8**(17), 4026–4034, DOI: 10.1039/d1qi00721a.

24 Y. Goto, M. Kikugawa, K. Kobayashi, T. Nanba, H. Matsumoto, K. Yamazaki, M. Matsumoto and H. Imagawa, Enhanced ammonia synthesis activity of Ru-supported cerium-lanthanum oxide induced by Ti substitution forming mesopores, *Chem. Commun.*, 2022, **58**(19), 3210–3213, DOI: 10.1039/d1cc07014b.

25 Y. Ma, G. Lan, W. Fu, Y. Lai, W. Han, H. Tang, H. Liu and Y. Li, Role of surface defects of carbon nanotubes on catalytic performance of barium promoted ruthenium catalyst for ammonia synthesis, *J. Energy Chem.*, 2020, **41**, 79–86, DOI: 10.1016/j.jechem.2019.04.016.

26 Z. Li, X. Zhang, L. Zhang, C. Xu and Y. Zhang, Pathway Alteration of Water Splitting via Oxygen Vacancy Formation on Anatase Titanium Dioxide in Photothermal Catalysis, *J. Phys. Chem. C*, 2020, **124**(48), 26214–26221, DOI: 10.1021/acs.jpcc.0c07117.

27 L. Zhang, R. Li, L. Cui, Z. Sun, L. Guo, X. Zhang, Y. Wang, Y. Wang, Z. Yu, T. Lei, X. Jian, X. Gao, C. Fan and J. Liu, Boosting photocatalytic ammonia synthesis performance over OVs-Rich Ru/W18O49: Insights into the roles of oxygen vacancies in enhanced hydrogen spillover effect, *Chem. Eng. J.*, 2023, **461**, 141892, DOI: 10.1016/j.cej.2023.141892.

28 Z. Xumei, Z. Qinmin, P. Yumei, M. Xiaoyan and F. Guangyin, Oxygen vacancies and morphology engineered Co3O4 anchored Ru nanoparticles as efficient catalysts for ammonia borane hydrolysis, *Int. J. Hydrogen Energy*, 2021, **47**(12), 7793–7801, DOI: 10.1016/j.ijhydene.2021.12.122.

29 W. Li, Y. Ye, S. Zhang, C. Liang and H. Zhang, A fluidized electrocatalysis approach for ammonia synthesis using

oxygen vacancy-rich Co3O4 nanoparticles, *Inorg. Chem. Front.*, 2021, **8**(17), 4026–4034, DOI: 10.1039/d1qi00721a.

30 P. Shu, X. Qi, Q. Peng, Y. Chen, X. Gong, Y. Zhang, F. Ouyang and Z. Sun, Heterogeneous metal trimer catalysts on Mo2TiC2O2 MXene for highly active N2 conversion to NH3, *Mol. Catal.*, 2023, **539**, 113036, DOI: 10.1016/j.mcat.2023.113036.

31 H. Jia, P. Jinjian, Y. Zhixiong and J. Xingmao, Enhanced ammonia synthesis activity of $Ru/Ba_5Ta_4O_{15}$ catalyst by reduction of Ba5Ta4O15 with CaH2, *Int. J. Hydrogen Energy*, 2022, **47**(65), 28019–28024, DOI: 10.1016/j.ijhydene.2022.06.123.

32 B. Lin, Y. Liu, L. Heng, X. Wang, J. Ni, J. Lin and L. Jiang, Morphology Effect of Ceria on the Catalytic Performances of Ru/CeO2 Catalysts for Ammonia Synthesis, *Ind. Eng. Chem. Res.*, 2018, **57**(28), 9127–9135, DOI: 10.1021/acs.iecr.8b02126.

33 Z. Ma, X. Xiong, C. Song, B. Hu and W. Zhang, Electronic metal-support interactions enhance the ammonia synthesis activity over ruthenium supported on Zr-modified CeO2 catalysts, *RSC Adv.*, 2016, **6**(56), 51106–51110, DOI: 10.1039/c6ra10540h.

34 A. Almontasser and A. Parveen, Probing the effect of Ni, Co and Fe doping concentrations on the antibacterial behaviors of MgO nanoparticles, *Sci. Rep.*, 2022, **12**(1), 7922, DOI: 10.1038/s41598-022-12081-z.

35 S. Zhao, Y. Yang, F. Bi, Y. Chen, M. Wu, X. Zhang and G. Wang, Oxygen vacancies in the catalyst: Efficient degradation of gaseous pollutants, *Chem. Eng. J.*, 2023, **454**, 140376, DOI: 10.1016/j.cej.2022.140376.

36 F. R. Garcia-Garcia, A. Guerrero-Ruiz and I. Rodriguez-Ramos, Role of B5-Type Sites in Ru Catalysts used for the NH3 Decomposition Reaction, *Top. Catal.*, 2009, **52**(6–7), 758–764, DOI: 10.1007/s11244-009-9203-7.

37 Z. Song, T. H. Cai, J. C. Hanson, J. A. Rodriguez and J. Hrbek, Structure and reactivity of Ru nanoparticles supported on modified graphite surfaces: A study of the model catalysts for ammonia synthesis, *J. Am. Chem. Soc.*, 2004, **126**(27), 8576–8584, DOI: 10.1021/ja031718s.

38 C. J. H. Jacobsen, S. Dahl, P. L. Hansen, E. Törnqvist, L. Jensen, H. Topsoe, D. V. Prip, P. B. Moenshaug and I. Chorkendorff, Structure sensitivity of supported ruthenium catalysts for ammonia synthesis, *J. Mol. Catal. A: Chem.*, 2000, **163**(1–2), 19–26, DOI: 10.1016/j.jcat.2004.12.005.

39 P. Yan, W. Guo, Z. Liang, W. Meng, Z. Yin, S. Li, M. Li, M. Zhang, J. Yan, D. Xiao, R. Zou and D. Ma, Highly efficient K-Fe/C catalysts derived from metal-organic frameworks towards ammonia synthesis, *Nano Res.*, 2019, **12**(9), 2341–2347, DOI: 10.1007/s12274-019-2349-0.

40 H. S. Zeng, K. Inazu and K. Aika, The working state of the barium promoter in ammonia synthesis over an active-carbon-supported ruthenium catalyst using barium nitrate as the promoter precursor, *J. Catal.*, 2002, **211**(1), 33–41, DOI: 10.1006/jcat.2002.3727.

41 Y. Baik, M. Kwen, K. Lee, S. Chi, S. Lee, K. Cho, H. Kim and M. Choi, Splitting of Hydrogen Atoms into Proton-Electron Pairs at BaO-Ru Interfaces for Promoting Ammonia Synthesis under Mild Conditions, *J. Am. Chem. Soc.*, 2023, **145**(20), 11364–11374, DOI: 10.1021/jacs.3c02529.

42 L. Wu, L. Su, Q. Liang, W. Zhang, Y. Men and W. Luo, Boosting Hydrogen Oxidation Kinetics by Promoting Interfacial Water Adsorption on d-p Hybridized Ru Catalysts, *ACS Catal.*, 2023, **13**(7), 4127–4133, DOI: 10.1021/acscatal.2c05547.

43 Y. Zheng, Q. Liu, C. Shan, Y. Su, K. Fu, S. Lu, R. Han, C. Song, N. Ji and D. Ma, Defective Ultrafine MnOx Nanoparticles Confined within a Carbon Matrix for Low-Temperature Oxidation of Volatile Organic Compounds, *Environ. Sci. Technol.*, 2021, **55**(8), 5403–5411, DOI: 10.1021/acs.est.0c08335.

44 B. Li, P. Xue, Y. Bai, Q. Tang, M. Qiao and D. Zhu, Coupling Cu doping and oxygen vacancies in Co_3O_4 for efficient electrochemical nitrate conversion to ammonia, *Chem. Commun.*, 2023, **59**(34), 5086–5089, DOI: 10.1039/d3cc00864a.

45 F. Jiang, S. Wang, B. Liu, J. Liu, L. Wang, Y. Xiao, Y. Xu and X. Liu, Insights into the Influence of CeO_2 Crystal Facet on CO2 Hydrogenation to Methanol over Pd/CeO2 Catalysts, *ACS Catal.*, 2020, **10**(19), 11493–11509, DOI: 10.1021/acscatal.0c03324.

46 Y. Qiao, S. Yang, X. Sun, C. Liu, Z. Liu, X. Li, L. Li, H. Liu and L. Wang, Tailoring local environment of oxygen vacancies by molybdenum doping on MnO2 for enhanced catalytic oxidation of VOCs, *Chem. Eng. J.*, 2024, **481**, 148703, DOI: 10.1016/j.cej.2024.148703.

47 C. S. Gopinath, S. G. Hegde, A. V. Ramaswamy and S. Mahapatra, Photoernission studies of polymorphic CaCO3 materials, *Mater. Res. Bull.*, 2002, **37**(7), 1323–1332, DOI: 10.1016/s0025-5408(02)00763-8.

48 W. Fei, L. Changming, Z. Xiaoyu, W. Min, G. E. David and D. Xue, Catalytic behavior of supported Ru nanoparticles on the {100}, {110}, and {111} facet of CeO_2, *J. Catal.*, 2015, **329**, 177–186, DOI: 10.1016/j.jcat.2015.05.014.

49 J. Chen, L. Wang, P. Wang and J. Cai, Catalytic properties of barium modified $Ru/MgZrO_2$ for the isomerization linoleic acid to conjugated linoleic acid, *J. Ind. Eng. Chem.*, 2019, **880**, 425–430, DOI: 10.1016/j.jiec.2019.08.022.

50 W. Li, P. Liu, R. Niu, J. Li and S. Wang, Influence of CeO_2 supports prepared with different precipitants over Ru/CeO_2 catalysts for ammonia synthesis, *Solid State Sci.*, 2020, **99**, 105983, DOI: 10.1016/j.solidstatesciences.2019.105983.

51 Z. Wang, Y. Ma and J. Lin, Ruthenium catalyst supported on high-surface-area basic ZrO_2 for ammonia synthesis, *J. Mol. Catal. A: Chem.*, 2013, **378**, 307–313, DOI: 10.1016/j.molcata.2013.07.003.

52 R. Belgamwar, R. Verma, T. Das, S. Chakraborty, P. Sarawade and V. Polshettiwar, Defects Tune the Strong Metal–Support Interactions in Copper Supported on Defected Titanium Dioxide Catalysts for CO_2 Reduction, *J. Am. Chem. Soc.*, 2023, **145**(15), 8634–8646, DOI: 10.1021/jacs.3c01336.

53 P. Seetharamulu, K. Hari Prasad Reddy, A. H. Padmasri, K. S. Rama Rao and B. David Raju, Role of promoters on highly active nano-Ru catalyst supported on Mg–Al

hydrotalcite precursor for the synthesis of ammonia, *Catal. Today*, 2008, **141**(1–2), 94–98, DOI: 10.1016/j.cattod.2008.05.010.

54 Z. Wang, J. Lin, R. Wang and K. Wei, Ammonia synthesis over ruthenium catalyst supported on perovskite type $BaTiO_3$, *Catal. Commun.*, 2012, **32**, 11–14, DOI: 10.1016/j.catcom.2012.11.024.

55 R. Wang, Y. Wang, M. Ren, G. Sun, D. Gao, Y. R. Chin Chong, X. Li and G. Chen, Effect of ceria morphology on the catalytic activity of Ru/ceria for the dehydrogenation of ammonia borane, *Int. J. Hydrogen Energy*, 2017, **42**(10), 6757–6764, DOI: 10.1016/j.ijhydene.2017.02.024.

56 M. Piacentini, M. Maciejewski and A. Baiker, Supported Pt-Ba NOx storage-reduction catalysts: Influence of support and Ba loading on stability and storage efficiency of Ba-containing species, *Appl. Catal., B*, 2006, **66**(1–2), 126–136, DOI: 10.1016/j.apcatb.2006.02.002.